Progress In Electromagnetics Research M, Vol. 58, 159–169, 2017

A GPU Implementation of the Inverse Fast Multipole Method for Multi-Bistatic Imaging Applications

Luis E. Tirado[1], Galia Ghazi[1], Yuri Álvarez-Lopez[2], Fernando Las-Heras[2], and José Á. Martinez-Lorenzo[1, *]

Abstract—This paper describes a parallel implementation of the Inverse Fast Multipole Method (IFMM) for multi-bistatic imaging configurations. NVIDIAs Compute Unified Device Architecture (CUDA) is used to parallelize and accelerate the imaging algorithm in a Graphics Processing Unit (GPU). The algorithm is validated with synthetic data generated by the Modified Equivalent Current Approximation (MECA) method and experimental data collected by a Frequency-Modulated Continuous Wave (FMCW) radar system operating in the 70–77 GHz frequency band. The presented results show that the IFMM implementation using the CUDA platform is effective at significantly reducing the algorithm computational time, providing a $300X$ speedup when compared to the single core OpenMP version of the algorithm.

1. INTRODUCTION

The use of millimeter wave imaging technology has been widely adopted to detect security threats, like Improvised Explosive Devices (IED), in airport checkpoints [1–6]. The images produced by such systems are often generated by backpropagating the scattered field in order to recover the reflectivity. There are two main requirements in electromagnetic imaging: fast calculation of the images, and accuracy. In general, reducing the calculation time requires considering free-space backpropagation models that might not be accurate at all (especially if the scattered field is acquired in the near field region). As a trade-off between accuracy and calculation time, acceleration schemes based on the Fast Multipole Method (FMM) [7, 8] have been developed.

The FMM is a forward operator that has been widely used in electromagnetics to enable fast calculation of the radiated field given the electromagnetic sources without jeopardizing result accuracy. It can be used in inverse problems (e.g., antenna diagnostics) based on iterative schemes that minimize a cost function [9, 10] to speed-up forward operations at each iteration. However, iterative schemes in inverse problems are still time-consuming if compared to the use of inverse operators. For this reason, an inverse operator derived from the FMM, the Inverse Fast Multipole Method (IFMM) has been presented in [11, 12] applied to inverse scattering and imaging problems.

The current implementation of IFMM using CPUs is computationally intensive when being evaluated at multiple frequencies and observation points for multiple transmitter and receiver configurations. Taking into account that the FMM has been efficiently implemented in Graphics Processing Units (GPUs) for efficient analysis of electromagnetic scattering problems [13] and acoustics [14], it is proposed to follow a similar methodology for the inverse operator, the IFMM, so that the computationally intensive parts of the IFMM code can be evaluated to the same accuracy at higher speeds by using a GPU.

Received 10 February 2017, Accepted 22 June 2017, Scheduled 18 July 2017

* Corresponding author: Jose Angel Martinez-Lorenzo (jmartinez@coe.neu.edu).
[1] Department of Electrical Engineering, Northeastern University, Boston, MA 02115, USA. [2] Department of Electrical Engineering, Area of Signal Theory and Communications, University of Oviedo, Gijn, Asturias, 33203, Spain.

Parallelization using GPUs is desired for the IFMM algorithm given that it can be used as an image reconstruction algorithm in a mm-wave concealed threat detection system. Solving this problem and generating real-time images is extremely important for a deployable system, including those operating in high-capacity mode [15–20]. The Department of Homeland Security (DHS), through its mission of preventing terrorism and enhancing security, requires a high throughput, non-invasive, accurate, and quick detection of person-borne threats in highly secure areas [1–3, 5, 6]. For this reason, it is essential to be able to process the scattered fields from the person under test into an accurate reconstruction as fast as possible. In this paper, the acceleration of the IFMM utilizing a GPU for different configurations of transmitter and receivers is presented and experimentally validated for a multi-bistatic radar configuration. The work is divided as follows: Section 2 gives an IFMM overview, Section 3 describes the GPU architecture and approaches used to speed up the IFMM code, while Section 4 details the performance of the algorithm with both simulated and measured data.

2. IFMM OVERVIEW

The IFMM algorithm is an inverse scattering technique [11], which may be used to reconstruct support and constitutive parameters of the object under test (OUT) from the acquired scattered field. The algorithm is based on backpropagating the scattered fields from the observation domain into the reconstruction or imaging domain to recover the reflectivity. The IFMM is derived from inverting a forward operator, the FMM. There are three IFMM operators: aggregation (1), translation (2), and disaggregation (3).

The first operator assumes that the scattered field, $E_m^{(q)}$ (where m and n indicate the measurement and polarization indexes), can be locally approximated as a plane wave. For this goal, the scattered field observation groups m_{obs} are defined. The phase-shift between the observation point r_m and the center of the m_{obs}-*th* observation group, $\vec{C}_{m_{obs}}$ is defined as $e^{+jk_0(\vec{r}_m-\vec{C}_{m_{obs}})}$. Similarly, the disaggregation operator assumes that the reflectivity, sometimes defined as equivalent currents, [11], $J_n^{(p)}$ (where n and p indicate the current and polarization index respectively in a cubic sub-domain $\Delta V_n'$) can be locally approximated as a plane wave within the source groups, n_{source}. The phase-shift between the center of the cubic sub-domain $\vec{r}_n'$ and the center of the n_{source}-*th* source group, $\vec{C}_{n_{source}}$ is defined as $e^{+jk_0(\vec{C}_{n_{source}}-\vec{r}_n')}$.

Finally, the translation operator backpropagates the field from the center of the observation groups $\vec{C}_{m_{obs}}$ to the center of the source groups $\vec{C}_{n_{source}}$, by means of a spherical wave expansion. It can be proved that if the distance between the observation and source groups meets the far field criteria, the main contribution comes from the unit vector $\hat{k}_{m_{obs},n_{source}}$, with the same direction as $\vec{C}_{m_{obs}}-\vec{C}_{n_{source}}$ [7, 8]. In the case of scattering problems, the far field criteria is fulfilled in most of the cases for all observation and source groups combinations, as explained in [11]. The indexes p, $q = 1, 2, 3$ in Eqs. (1)–(3) subsequently designate x, y, and z polarization for the following IFMM operators:

$$iA^{(p)}_{m_{obs},n_{source}} = C_0 \cdot \sum_{q=1}^{3} \left\{ \sum_{m=1}^{M_{m\,obs}} K^{(p,q)}_{m_{obs},n_{source}} e^{+jk_0(\vec{r}_m-\vec{C}_{m_{obs}})\cdot\hat{k}_{m_{obs},n_{source}}} \cdot E_m^{(q)} \right\} \tag{1}$$

$$iT^{(p)}_{m_{obs},n_{source}} = iA^{(p)}_{m_{obs},n_{source}} \cdot 4\pi jk_0 \left|\vec{C}_{m_{obs}}-\vec{C}_{n_{source}}\right| e^{+jk_0\left|\vec{C}_{m_{obs}}-\vec{C}_{n_{source}}\right|} \tag{2}$$

$$J_n^{(p)} = \sum_{m_{obs}=1}^{M_{obs}} e^{+jk_0(\vec{C}_{n_{source}}-\vec{r}_n')\cdot\hat{k}_{m_{obs},n_{source}}} \cdot iT^{(p)}_{m_{obs},n_{source}} \cdot \Delta V_n', \tag{3}$$

where $\left|\vec{C}_{m_{obs}}-\vec{C}_{n_{source}}\right|$ is the distance from the center of the m_{obs}-*th* observation group $\vec{C}_{m_{obs}}$ to the center of the n_{source}-*th* source group $\vec{C}_{n_{source}}$. The $K^{(p,q)}_{m_{obs},n_{source}}$ dyadic term is defined and described in [11], $C_0 = -\eta(k_0/4\pi)^2$, η is the wave impedance, and the indexes in the previous equations are defined as follows [11]:

$$m_{obs} = 1, \ldots, M_{obs} \quad n_{source} = 1, \ldots, N_{source} \tag{4}$$

$$m = 1, \ldots, M_{m_{obs}} \quad n = 1, \ldots, N_{source} \tag{5}$$

$$\vec{r}_m \in M_{m_{obs}} \quad J_n^{(p)}, \vec{r}\,'_n, \Delta V'_n \in N_{n_{source}}, \tag{6}$$

where M is the number of observation points, $M_{m_{obs}}$ the number of elements in the m_{obs}-th observation group, M_{obs} the number of observation groups, N the number of source points, $N_{n_{source}}$ the number of elements in the n_{source}-th source group, and N_{source} the number of source groups. A graphic representation of the IFMM algorithm can be seen in Fig. 1.

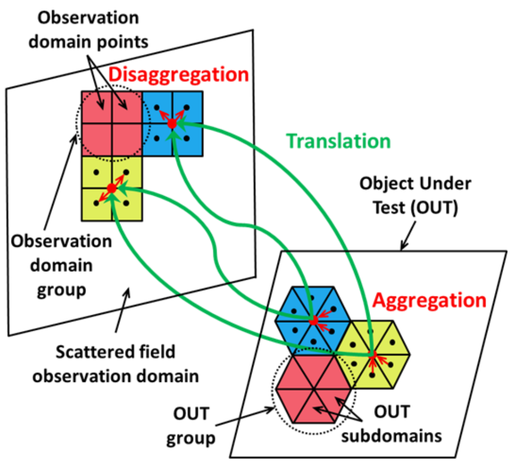

Figure 1. IFMM scattered field observation and reconstruction (OUT) domains.

As explained in [11], the use of plane wave and spherical wave expansions is more accurate than the free-space backpropagation approach used in conventional SAR imaging (that can be speed up using Inverse Fast Fourier Transforms).

Concerning FMM and IFMM implementation, there is an important difference mainly due to the kind of problem (forward/inverse) where these acceleration schemes are used. FMM has been mostly used in forward scattering problems [7, 8], where the presence of near-field groups (i.e., observation and source groups adjacent to each other) requires the use of conventional MoM. Besides, if the far field distance is not met for a pair of observation-source groups, the translation operator, which is based on an spherical wave expansion, limits FMM speedup. This results in a more complex GPU implementation.

IFMM is applied in inverse problems [11, 12], where in the majority of the cases the observation and source domains are physically different (as observed in Fig. 1), so the far field condition for each pair of observation-source groups is fulfilled. Thanks to this the translation operator can be reduced to a single spherical wave mode, which simplifies GPU implementation of IFMM, as it will be described in Section 3.

3. GPU IMPLEMENTATION DETAILS

3.1. Kepler CUDA Architecture

The Kepler architecture in the GTX Titan Black GPU is a consumer-available GPU hardware developed by NVIDIA which offers full-speed double precision computations [21]. Comprised of 7.1 billion transistors, it leverages Single-Instruction Multiple-Data (SIMD) parallelism, providing a maximum of 1.4 TFLOPS of double precision computing power distributed over 15 Streaming Multiprocessor (SMX) units and six 64-bit memory controllers. Each SMX unit consists of various execution units (EUs): 192 single-precision CUDA cores, 64 double-precision units, 32 special function units (SFU) used for transcendental operations, and 32 load/store units (LD/ST). A CUDA program calls one or more kernels, which are functions that are executed on the GPU using the specified threads and blocks. A thread on the GPU is the basic element of the data to be processed. Threads are organized into thread blocks and grids of thread blocks. An SMX executes at least one thread block, and CUDA cores and other EUs in the SMX execute corresponding thread instructions. A challenge in implementing the IFMM on NVIDIA CUDA enabled GPUs is to make the most effective use of the platforms resources.

3.2. IFMM CUDA C Implementation

An existing and validated OpenMP version of the IFMM code was used to implement the CUDA C version. In the OpenMP IFMM version, the aggregation, translation, and disaggregation operations in Eqs. (1)–(3) are done via nested loops.

An initial version of the CUDA code used a 1D kernel for the aggregation operation and a separate 2D kernel for the translation operation. However, because the 1D kernel's inner loop iterated over $M_{obs} \gg M_{m_{obs}}$, a lesser amount of parallelism was exploited. Therefore, the execution time was slower. The optimized approach computes the aggregation and translation steps described in Eqs. (1), (2) jointly, which avoids delays associated with additional kernel launches [22].

The disaggregation step from Eq. (3) is performed as a separate kernel. In its initial version, the disaggregation kernel used 2D indexing elements which corresponded to N_{source} and $N_{n_{source}}$. This kernel was launched with $\max(n_{source})$ threads. Given the number of elements in each n_{source} group can vary, some launched threads can terminate without doing work due to being out of bounds. These terminated threads consume GPU resources that would otherwise be expended on threads that perform computations, thus increasing the overall execution time. The optimized disaggregation kernel uses 1D indexing based on N, the total number of source points, to avoid this issue.

A further optimization involves loading the 2D input variables into GPU memory as 1D flattened arrays in row-major format. This allows concurrent threads to simultaneously access adjacent memory addresses within the physical GPU memory. In this way, the GPU hardware is able to combine memory accesses which increases effective memory bandwidth [23]. Additionally, accessing data from 1D arrays is faster, as it avoids the cost of global memory reads associated with pointer indirections.

The IFMM aggregation/translation and disaggregation kernels are launched with 256 threads per thread block in order to ensure a fast execution time. For both kernels, the occupancy of each multiprocessor is limited by the number of registers used by the kernels. In an attempt to increase occupancy, both kernels were launched with a larger number of threads per block given the input data sets detailed in Section 4. However, given that these kernels are compute-bound, this approach results in the same or a slower execution time [24].

The output of the optimized aggregation and translation kernel is an $M_{obs} \times N_{source}$ array, so it is advantageous to arrange the 256 threads in each thread block into a 16×16 2D grid to take advantage

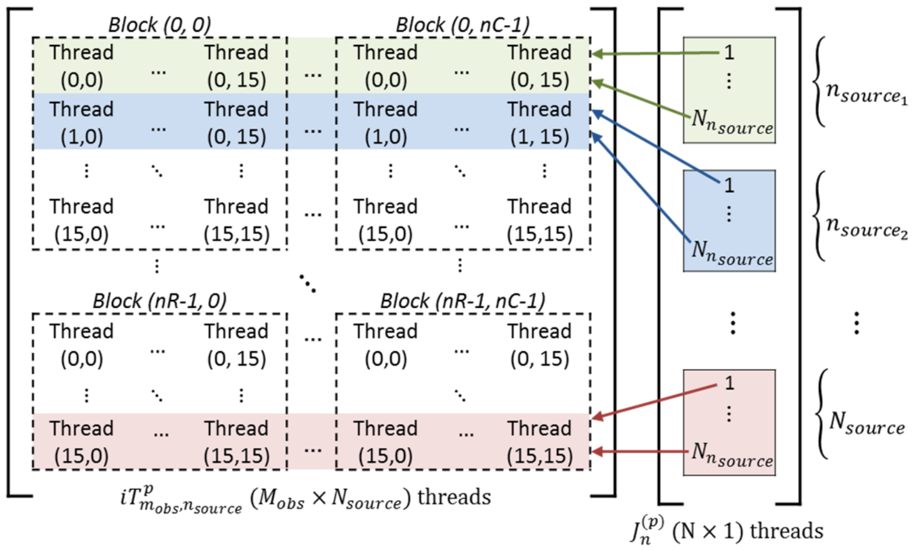

Figure 2. Arrangement of threads and blocks for IFMM Aggregation/Translation & Disaggregation kernels.

of CUDA's grid structure [25]. Each thread in the kernel calculates a 2D index pair as follows:

$$xIdx = blockDim.x * blockIdx.x + threadIdx.x \tag{7}$$

$$yIdx = blockDim.y * blockIdx.y + threadIdx.y \tag{8}$$

where *threadIdx.x* and *threadIdx.y* vary from [0, 15], and *blockDim.x*=*blockDim.y*=16. Each thread iterates over $M_{m_{obs}}$, the number of elements of each observation group, to calculate one element of the output matrix. For the aggregation/translation kernel, the thread block dimensions *blockIdx.x* and *blockIdx.y* vary from $[0, nR-1]$ and $[0, nC-1]$, respectively.

The optimized disaggregation kernel arranges the 256 threads within each thread block in 1D, such that only Eq. (7) is used to index each thread. Thus, *threadIdx.x* varies from $[0, 255]$ and $blockDim.x = 256$. This kernel launches N threads that iterate over M_{obs}, each of which computes the *n-th* equivalent current utilizing the output of the combined aggregation/translation kernel. Fig. 2 shows the arrangement of threads and blocks used to compute the $iT^{p}_{(m_{obs},n_{source})}$ and $J^{(p)}_n$ arrays. Each source point within a specific source group in the disaggregation kernel utilizes one column of data from the matrix computed by the aggregation/translation kernel.

For the CUDA version of the IFMM code, the kernels are batched consecutively, each set adding the results for the currents $J^{(p)}_n$ over the multiple processed frequencies. For example, processing a data-set with 32 frequencies means that 64 kernels will be executed -32 for the aggregation/disaggregation and 32 for the disaggregation operation. The process is summarized in the following pseudo-code:

```
For frequency from 1 to $F_n$:
  (i) Launch 2D aggregation/translation kernel with $M_{obs} \times N_{source}$ threads, divided into $nC \times nR$ thread blocks. Each thread:
      (a) Operates on a unique observation/source group.
      (b) Iterates over $M_{m_{obs}}$ and computes vector $\vec{r}_m - \vec{C}_{m_{obs}}$ and the scalar/complex products of Eq. (1).
      (c) Keeps result in GPU memory and uses it to calculate products of Eq. (2).
      Output: $iT^{(p)}_{m_{obs},n_{source}}$, an $M_{obs} \times N_{source}$ array.
  (ii) Launch 1D disaggregation kernel with $N$ threads divided into $nR$ thread blocks. Each thread:
      (a) Determines which source group the current source belongs to and computes vector $\vec{C}_{n_{source}} - \vec{r}'_n$.
      (b) Iterates over $M_{obs}$ and performs scalar/complex products in Eq. (3) using $iT^{(p)}_{m_{obs},n_{source}}$ and accumulates their sum.
      Output: $J^{(p)}_n$, $N$ currents, matching to each source point.
  (iii) Keep a cumulative sum for each of the $N$ currents.
End
```

4. APPLICATION EXAMPLES

The validation examples in this work were conducted with the CUDA IFMM code using a single workstation 3.4 GHz Intel® Core™ i7-4930K hexa-core CPU with an NVIDIA GeForce® GTX Titan Black GPU with 6 GB of GDDR5 VRAM connected via a PCI-E 3.0×16 interface. This GPU contains 2880 CUDA cores, running at a base clock of 967 MHz. The IFMM OpenMP and CUDA codes were compiled with GCC/G++ 4.6.4. The CUDA 5.5 toolkit was used, and codes were profiled under 64-bit Ubuntu 14.04 with NVIDIA 337 drivers.

The CUDA implementation was validated against the OpenMP version for numerical accuracy and shown to match exactly. IFMM code has been previously validated against our traditional Synthetic Aperture Radar (SAR) method [26], for this reason the same comparison is not included in this work, which focuses on the speed improvements of the IFMM algorithm. Three experiments are included in this section: the first two make use of synthetic data to perform the imaging, while the last one used measured data for the same purpose.

4.1. Simulation-Based Experiments

For performance tests, two data sets spanning the 70–77 GHz frequency range with varying input parameters are used. These sets (Experiment 1 & 2) use a tessellated model of the human body, composed of 9320 facets, as the object under test (OUT). The transmitting and receiving arrays are located 1.5m away from the body. The scattered electric field data $E_m^{(q)}$ in Eq. (1) is calculated via the MECA method [27]. In Experiment 1, receivers are arranged every $\lambda/2$ in a 1.5 m × 1.5 m grid and 4 transmitters are employed at the grid corners. In Experiment 2, 1538 receivers are distributed into 2 horizontal lines, with the transmitters in a vertical line, once again arranged with a $\lambda/2$ spacing. The geometries for the experiments are shown in Figs. 3(a) and 3(b). The position of the transmitters and receivers in these figures is denoted by (Tx, Ty, Tz) and (Rx, Ry, Rz), respectively. Bx, By, and Bz denote the size of the minimum box enclosing the OUT (human body). For both experiments, the human body is discretized into 116 slices in the Z-direction, (0.05 m to 1.775 m) each of which is generated

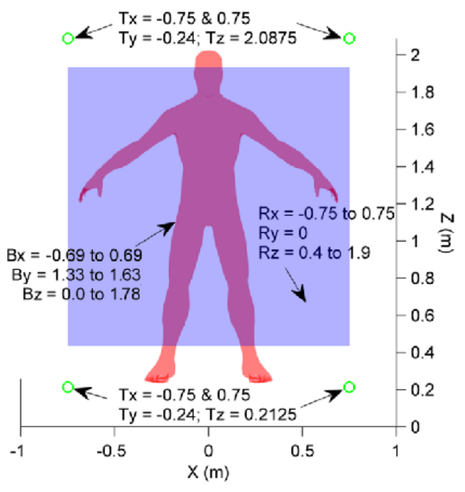

(a)

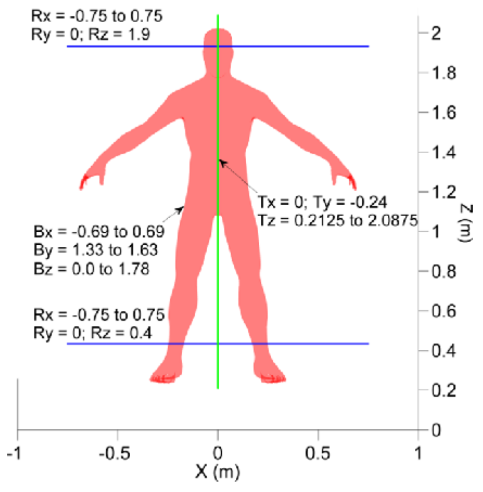

(b)

Figure 3. IFMM experiment geometry sketches. (a) Sketch of geometry for IFMM Experiment 1. (b) Sketch of geometry for IFMM Experiment 2.

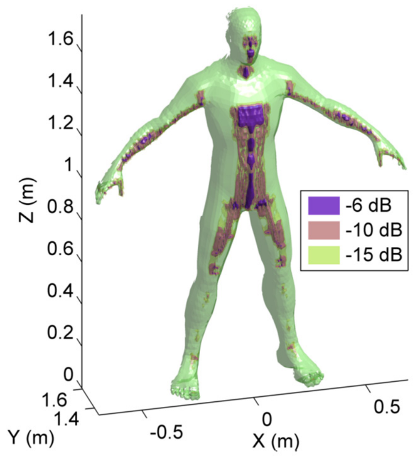

(a)

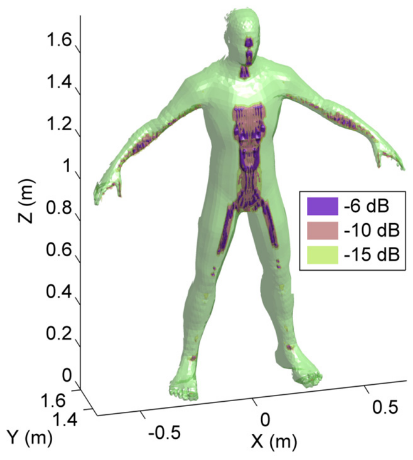

(b)

Figure 4. IFMM experiments: recovered reflectivity levels. (a) IFMM Experiment 1: Recovered reflectivity levels at −6, −10, and −15 dB. (b) IFMM Experiment 2: Recovered reflectivity levels at −6, −10, and −15 dB.

by the IFMM code for every transmitter. Each 687×129 pixels slice spans $X = [-0.67\,\mathrm{m}\,0.67\,\mathrm{m}]$ and $Y = [1.325\,\mathrm{m}\,1.575\,\mathrm{m}]$. The contributions for each transmitter are added non-coherently to produce the final reconstruction. Figs. 4(a) and 4(b) show the IFMM reconstruction results overlaid over the human body model for Experiments 1 and 2, respectively. Despite the different receiver/transmitter configurations, both methods produce similar images given the array geometry correspondence [28]. The nR and nC values for each of the IFMM reconstructions are listed in Table 1. Table 2 lists the IFMM input parameters used in evaluating the two simulation-based examples, as well as a measured data reconstruction.

Table 1. IFMM kernel launch parameters.

Operation	# of kernel thread blocks	Exp. 1	Exp. 2	Exp. 3
CUDA Aggregate w/Translate	$nR = \left\lceil \frac{N_{source}}{16} \right\rceil$	158	158	185
	$nC = \left\lceil \frac{M_{obs}}{16} \right\rceil$	1859	23	7
CUDA Disaggregate	$nR = \left\lceil \frac{N}{256} \right\rceil$	347	347	83
	$nC = 1$ (1D kernel)	1	1	1

Table 2. IFMM input parameters per slice.

Parameters	Exp. 1 — Simul.	Exp. 2 — Simul.	Exp. 3 — Meas.
M (obs. points)	591361	1538	451
N (source points)	88623	88623	21115
M_{obs}	29736	354	101
N_{source}	2528	2528	2945
# of frequencies	32	32	731
$\max(N_{n\,source})$	45	45	12
$\max(M_{m\,obs})$	25	5	5

4.2. Measurement-Based Experiments

The third IFMM data set (Experiment 3) was collected with the 70–77 GHz Radar Front End (RFE) Model 8300 developed by the company HXI [29]. The data was collected by two receivers, indicated by $R \times 1$ and $R \times 2$ in Fig. 5, while a transmitter is moved by a linear actuator over a straight line. An AlazarTech ATS9870 digitizer card was used to capture the data. The OUT is a 91.5 cm long steel rod of 2.5 cm in diameter, located in front of a metallic plate. A top-down view of the steel plate and rod with a foam piece behind as support is shown in Fig. 6. The images for Experiment 3 are reconstructed on a single 205×103 pixels slice ($z = 0.954\,\mathrm{m}$), spanning $X = [-0.4\,\mathrm{m}\,0.4\,\mathrm{m}]$ and $Y = [1.3\,\mathrm{m}\,1.7\,\mathrm{m}]$; the

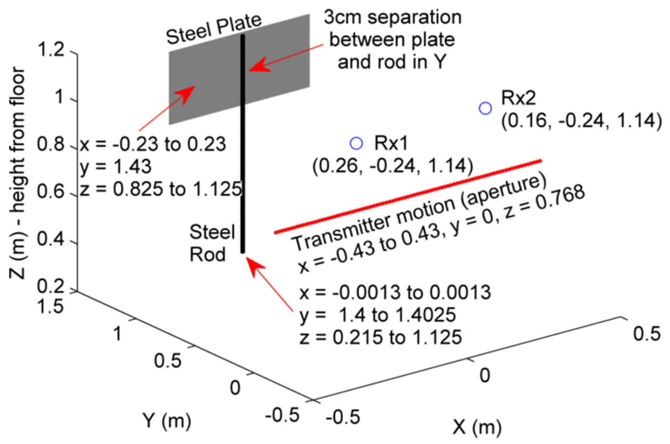

Figure 5. Sketch of geometry for measured data IFMM Experiment 3.

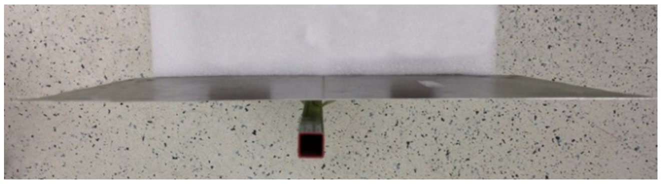

Figure 6. Top down view of steel plate and rod for Experiment 3.

21115 pixels are grouped into 2945 source groups — see the fourth column in Table 2. The scattered data is observed at 451 positions, which are grouped into 101 observation groups. Fig. 7 presents 2D images of the OUT, at the $z = 0.954m$ plane, when the imaging is performed using the field measured by only the first receiver, by only the second receiver, and by both receivers.

4.3. Performance Evaluation

Table 3 shows the timing figures of the IFMM OpenMP implementation with 12 threads against the GTX Titan Black GPU CUDA code. The speedup factor of IFMM on the GPU versus the CPU counterpart is largely tied to the number of kernel thread blocks launched by the different data sets. For a larger amount of blocks used, the speedup is maximized, given that a larger level of parallelism is exploited. The IFMM CUDA code on the GTX Titan Black, which generates exactly the same image as the C-based version is able to achieve for Experiments 1, 2, and 3, respectively, the following speedups: 36X, 41X, and 20X, when compared to the OpenMP 12-core CPU version of the code; and 267X, 308X, and 157X, when compared to the 1-core CPU version of the code. Concerning numerical precision, results provided by CPU and GPU implementations were compared; the maximum normalized root mean square error observed for the experiments is below 1e-16.

Table 3. IFMM computation times per slice and transmitter.

IFMM	Time (ms)		
modality	Exp. 1	Exp. 2	Exp. 3
CUDA GPU	378	34879	1301
12-core CPU	13809	1462263	27215
1-core CPU	100865	10746589	205295

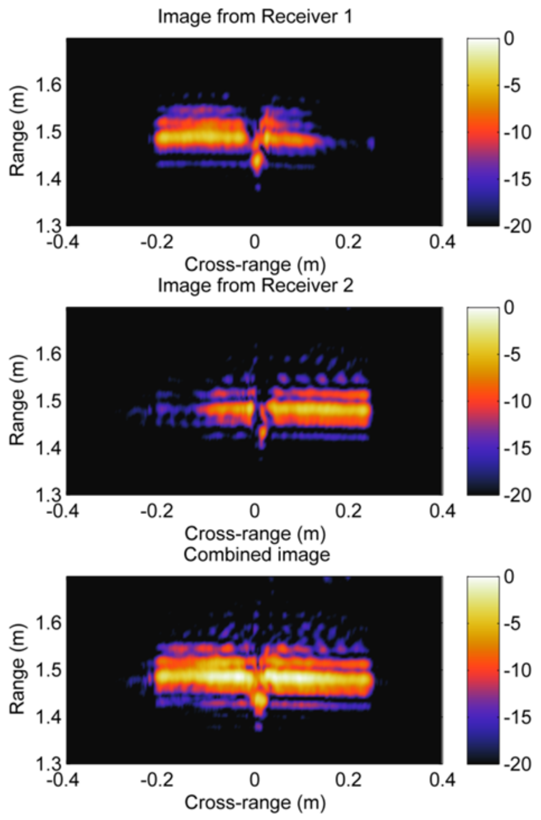

Figure 7. Experiment 3 Reconstructed images: receiver 1 (top), receiver 2 (center), and non-coherent combination of both receivers (bottom). Normalized reflectivity, in dB.

5. CONCLUSION

This paper describes a CUDA implementation of the multi-static IFMM code, which has the potential to be used for real-time imaging of security threats. The performance of the OpenMP-based and the CUDA-based versions of the IFMM code has been evaluated using both synthetic and experimental datasets. In both cases, the CUDA-based version of the algorithm outperforms the OpenMP-based version, in terms of computational cost, without degrading the quality of the reconstructed image. The extension of the IFMM to operate with multiple levels, as it is often done by Multi-Level Fast Multipole Algorithms, will be studied in our future work.

ACKNOWLEDGMENT

This material is based upon work supported by the Science and Technology Directorate, U.S. Department of Homeland Security, Award No. 2013-ST-061-ED0001; by the "Ministerio de Economía y Competitividad" of Spain under project TEC2014-54005P (MIRIIEM); and by the "Gobierno del Principado de Asturias" under project GRUPIN14-114.

REFERENCES

1. Sheen, D., D. McMakin, and T. Hall, "Three-dimensional millimeter-wave imaging for concealed weapon detection," *IEEE Transactions on Microwave Theory and Techniques*, Vol. 49, No. 9, 1581–1592, 2001.
2. Ahmed, S. S., A. Schiessl, F. Gumbmann, M. Tiebout, S. Methfessel, and L. P. Schmidt, "Advanced microwave imaging," *IEEE Microwave Magazine*, Vol. 13, No. 6, 26–43, Sep. 2012.

3. Martinez-Lorenzo, J. A., F. Quivira, and C. M. Rappaport, "SAR imaging of suicide bombers wearing concealed explosive threats," *Progress In Electromagnetics Research*, Vol. 125, 255–272, 2012.
4. Alvarez, Y., B. Gonzalez-Valdes, J. Martinez Lorenzo, F. Las-Heras, and C. Rappaport, "3d whole body imaging for detecting explosive-related threats," *IEEE Transactions on Antennas and Propagation*, Vol. 60, No. 9, 4453–4458, 2012.
5. Gonzalez-Valdes, B., Y. Alvarez, Y. Rodriguez-Vaqueiro, A. Arboleya-Arboleya, A. Garcia-Pino, C. M. Rappaport, F. Las-Heras, and J. A. Martinez-Lorenzo, "Millimeter wave imaging architecture for on-the-move whole body imaging," *IEEE Transactions on Antennas and Propagation*, Vol. 64, No. 6, 2328–2338, Jun. 2016.
6. Gonzalez-Valdes, B., C. Rappaport, J. A. M. Lorenzo, Y. Alvarez, and F. Las-Heras, "Imaging effectiveness of multistatic radar for human body imaging," *2015 IEEE International Symposium on Antennas and Propagation USNC/URSI National Radio Science Meeting*, 681–682, Jul. 2015.
7. Coifman, R., V. Rokhlin, and S. Wandzura, "The fast multipole method for the wave equation: a pedestrian prescription," *IEEE Antennas and Propagation Magazine*, Vol. 35, No. 3, 7–12, Jun. 1993.
8. Darve, E., "The fast multipole method: Numerical implementation," *Journal of Computational Physics*, Vol. 160, No. 1, 195–240, 2000, [Online], Available: http://www.sciencedirect.com/science/article/pii/S0021999100964519.
9. Eibert, T. F. and C. H. Schmidt, "Multilevel fast multipole accelerated inverse equivalent current method employing rao-wilton-glisson discretization of electric and magnetic surface currents," *IEEE Transactions on Antennas and Propagation*, Vol. 57, No. 4, 1178–1185, Apr. 2009.
10. Alvarez-Lopez, Y., F. Las-Heras, M. R. Pino, and J. A. Lopez, "Acceleration of the sources reconstruction method via the fast multipole method," *2008 IEEE Antennas and Propagation Society International Symposium*, 1–4, Jul. 2008.
11. Alvarez, Y., J. A. Martinez-Lorenzo, F. Las-Heras, and C. M. Rappaport, "An inverse fast multipole method for geometry reconstruction using scattered field information," *IEEE Transactions on Antennas and Propagation*, Vol. 60, No. 7, 3351–3360, 2012.
12. Schnattinger, G. and T. F. Eibert, "Solution of the vectorial 3d inverse source problem by adjoint near-field fast multipole translations," *Proceedings of the 2012 IEEE International Symposium on Antennas and Propagation*, 1–2, Jul. 2012.
13. Dang, V., Q. Nguyen, and O. Kilic, "Gpu cluster implementation of fmm-fit for large-scale electromagnetic problems," *IEEE Antennas and Wireless Propagation Letters*, Vol. 13, 1259–1262, 2014.
14. López-Portugués, M., J. A. López-Fernández, J. Menéndez-Canal, A. Rodríguez-Campa, and J. Ranilla, "Acoustic scattering solver based on single level fmm for multi-gpu systems," *J. Parallel Distrib. Comput.*, Vol. 72, No. 9, 1057–1064, Sep. 2012, [Online], Available: http://www.sciencedirect.com/science/article/pii/S0743731511001481.
15. Martinez-Lorenzo, J., J. Heredia Juesas, and W. Blackwell, "A single-transceiver compressive reflector antenna for high-sensing-capacity imaging," *IEEE Antennas and Wireless Propagation Letters*, Vol. PP, No. 99, 1–1, 2015.
16. Molaei, A., G. Allan, J. Heredia, W. Blackwell, and J. Martinez-Lorenzo, "Interferometric sounding using a compressive re ector antenna," *2016 10th European Conference on Antennas and Propagation (EuCAP), IEEE*, 1–4, 2016.
17. Juesas, J. H., G. Allan, A. Molaei, L. Tirado, W. Blackwell, and J. A. M. Lorenzo, "Consensus-based imaging using admm for a compressive re ector antenna," *2015 IEEE International Symposium on Antennas and Propagation* & *USNC/URSI National Radio Science Meeting, IEEE*, 1304–1305, 2015.
18. Obermeier, R. and J. A. Martinez-Lorenzo, "Model-based optimization of compressive antennas for high-sensing-capacity applications," *IEEE Antennas and Wireless Propagation Letters*, Vol. PP, No. 99, 1–1, 2016.

19. Wang, L., L. Li, Y. Li, H. C. Zhang, and T. J. Cui, "Single-shot and single-sensor high/super-resolution microwave imaging based on metasurface," *Scientific Reports*, Vol. 6, 26959, 2016.
20. Gopalsami, N., S. Liao, T. W. Elmer, E. R. Koehl, A. Heifetz, A. C. Raptis, L. Spinoulas, and A. K. Katsaggelos, "Passive millimeter-wave imaging with compressive sensing," *Optical Engineering*, Vol. 51, No. 9, 091 614-1, 2012.
21. "Nvidia's next generation cuda compute architecture: Kepler gk110/210," http://international.download.nvidia.com/pdf/kepler/nvidia-kepler-gk110-gk210-architecture-whitepaper.pdf, 2014.
22. Boyer, M., "Cuda kernel overhead," http://www.cs.virginia.edu/∼mwb7w/cuda support/kernel overhead.html, online, accessed Apr. 7, 2017.
23. Harris, M., "How to access global memory efficiently in cuda c/c++ kernels," NVIDIA, Jan. 2013, [Online], Available: https://devblogs.nvidia.com/parallelforall/how-access-global-memory-efficiently-cuda-c-kernels/24,
24. "Nvidia, cuda occupancy calculator," http://developer.download.nvidia.com/compute/cuda/cuda occupancy calculator.xls," 2012.
25. Kirk, D. B. and W.-M. W. Hwu, *Programming Massively Parallel Processors: A Hands-on Approach*, 3rd edition, Morgan Kaufmann Publishers Inc., San Francisco, CA, USA, 2016.
26. Alvarez, Y., J. Laviada, L. Tirado, C. Garcia, J. Martinez, F. Las-Heras, and C. M. Rappaport, "Inverse fast multipole method for monostatic imaging applications," *IEEE Geoscience and Remote Sensing Letters*, Vol. 10, No. 5, 1239–1243, Sep. 2013.
27. Meana, J., J. Á. Martínez-Lorenzo, F. Las-Heras, and C. Rappaport, "Wave scattering by dielectric and lossy materials using the modified equivalent current approximation (MECA)," *IEEE Transactions on Antennas and Propagation*, Vol. 58, No. 11, 3757–3761, 2010.
28. Ahmed, S. S., A. Schiessl, and L. P. Schmidt, "Multistatic mm-wave imaging with planar 2d-arrays," *2009 German Microwave Conference*, 1–4, Mar. 2009.
29. "Hxi model 8300 73 GHz multi-static FMCW radar front end (RFE)," http://www.hxi.com/Products/hfnov12.pdf, 2012.